



This is a repository copy of *Spherical equivalence of cylindrical explosives: Effect of charge shape on deflection of blast-loaded plates*.

White Rose Research Online URL for this paper:
<https://eprints.whiterose.ac.uk/173508/>

Version: Accepted Version

Article:

Rigby, S. orcid.org/0000-0001-6844-3797, Osborne, C., Langdon, G. et al. (2 more authors) (2021) Spherical equivalence of cylindrical explosives: Effect of charge shape on deflection of blast-loaded plates. *International Journal of Impact Engineering*, 155. 103892. ISSN 0734-743X

<https://doi.org/10.1016/j.ijimpeng.2021.103892>

Article available under the terms of the CC-BY-NC-ND licence
(<https://creativecommons.org/licenses/by-nc-nd/4.0/>).

Reuse

This article is distributed under the terms of the Creative Commons Attribution-NonCommercial-NoDerivs (CC BY-NC-ND) licence. This licence only allows you to download this work and share it with others as long as you credit the authors, but you can't change the article in any way or use it commercially. More information and the full terms of the licence here: <https://creativecommons.org/licenses/>

Takedown

If you consider content in White Rose Research Online to be in breach of UK law, please notify us by emailing eprints@whiterose.ac.uk including the URL of the record and the reason for the withdrawal request.



eprints@whiterose.ac.uk
<https://eprints.whiterose.ac.uk/>

Spherical equivalence of cylindrical explosives: Effect of charge shape on deflection of blast-loaded plates

S.E. Rigby^{a,*}, C. Osborne^a, G.S. Langdon^a, S.B. Cooke^b, D.J. Pope^b

^aDepartment of Civil & Structural Engineering, University of Sheffield, Mappin Street, Sheffield, S1 3JD, UK

^bPhysical Sciences Group, Platform Services Division, DSTL Porton Down, Salisbury, Wiltshire, SP4 0JQ, UK.

Abstract

Quantification of near-field blast loading is a pressing issue for defence, transport security, and structural engineering. Realistic explosion scenarios often involve the detonation of non-spherical high explosive charges, rather than the idealised spherical/hemispherical explosives assumed in commonly employed semi-empirical approaches. Additionally, near-field effects are of great importance when assessing structural damage and injury risk from such an event. There is a need, therefore, to incorporate the effects of charge shape and the resulting loading distribution in simplified engineering-level tools using adjustments based on sound physical principles. This article details the development of an energy equivalent formulation to derive spherical equivalence factors, with the methodology illustrated for the scenario of a centrally detonated cylindrical explosive charge. A validated two-part numerical model is used to generate specific impulse distributions and quantify the resulting plate deformation, for a wide range of cylindrical aspect ratios ($0.20 \leq L/D \leq 5$), at a range of near-field scaled distances ($0.108 \leq Z \leq 0.485 \text{ m/kg}^{1/3}$) for different sized structural targets. A series of verification examples are used to demonstrate the accuracy of the method, with the peak deflection under the equivalent spherical charge matching peak deflection under the cylindrical charge to within $\sim 4\%$. The method developed in this article could be extended to find equivalence between any two systems with complex distributed loading, allowing for a fast running engineering approximation in cases where detailed modelling is inappropriate or infeasible.

Keywords: Blast loading, Cylindrical explosive, Energy equivalent impulse, Kinetic energy uptake, Plate deflection, Spherical equivalence

*Tel.: +44 (0) 114 222 5725

Email address: sam.rigby@shef.ac.uk (S.E. Rigby)

1. Introduction

Prediction of blast loading is a critical first step in assessing the performance of protective systems and critical infrastructure against the effects of near-field explosions. There is a pressing need to better understand the fundamental processes governing the development of blast loads on a structure, and subsequent structural response, in order to provide the engineering community with simple predictive tools based on physically valid principles. Determining peak dynamic deflection is necessary in applications such as armoured vehicle design [1], assessment of perimeter walls against vehicle-borne explosives [2], and the provision of protected spaces within buildings [3]. High-fidelity numerical schemes are not yet suitable (on account of computational cost) for use in risk-based analyses which require the consideration of a wide range of input parameters, however their ability to provide key insights into mechanistic behaviour makes them highly suitable for informing the development of quick running tools.

Existing methods for predicting blast loading on a structure, e.g. those based on the analytical work of Brode [4] or the Kingery/Kingery & Bulmash semi-empirical relations [5, 6] (implemented into the computer code ConWep [7]), are known to be accurate for relatively simple geometric scenarios [8]. However, such methods are based on the assumption that the explosive is either formed into a sphere and detonated in free air, or formed into a hemisphere and detonated on the ground. Whilst these scenarios are suitable for fundamental scientific studies of blast wave development, it is rare that a real-life explosive device will conform to this idealisation. It is necessary, therefore, to understand the loading from a non-spherical explosive in order to supplement existing and improved predictive methodologies (e.g. [9]) with spherical equivalence factors. The aim of this study is to provide a series of simple adjustment factors to allow users to model the effects of a non-spherical explosive whilst using engineering-level simplified tools.

When a spherical explosive detonates the wave front reaches all edges of the explosive concurrently and the blast wave expands into the air in a spherically symmetric manner. Conversely, the detonation wave in a cylindrical charge will not reach all edges of the explosive at the same instant in time and the resultant shape of the blast wave is highly complex due to differing levels of inertial confinement offered by the uninitiated explosive material. This results in separate primary waves emanating from the ends and sides of the explosive, with secondary bridging waves formed where the two meet [10]. Hence, it is well known that peak overpressure and specific impulse from cylindrical explosives are dependent on azimuth angle [11], i.e. the angle between the longitudinal axis of the

cylinder and the measurement axis [12].

A critical factor that governs the initial shape and subsequent expansion of a blast wave from a cylindrical explosive is the aspect ratio, i.e. the ratio between the length (or height) of the charge, and its diameter: L/D . Plooster [13] reviewed and analysed available experimental data [14, 15] to derive multi-parameter curve fits to estimate incident overpressure as a function of scaled distance, L/D , and azimuth angle. This work was later developed by Esparza [12] to include additional experimental results [16] which tested a larger range of L/D and scaled distances, from which pressure and impulse amplitude ratio curves were derived for certain azimuth angles. The results showed that the enhancement factor (that is the equivalent spherical mass required to impart the same load as a unit cylindrical charge mass) varied between ~ 0.3 and ~ 18 as a function of scaled distance, aspect ratio and azimuth angle, although the experimental results were only available for mid-field conditions, $Z > 1.24 \text{ m/kg}^{1/3}$.

Simoens and Lefebvre [17] experimentally measured mid- to far-field incident blast pressure from spherical explosives and cylinders of different aspect ratios and found a range of spherical equivalence factors between 0.8–1.8 (when considering incident pressure) and 0.6–1.4 (when considering incident specific impulse). Wu et al. [18] used finite element analysis to undertake a parametric study on (among others) the effect of L/D , charge orientation, and scaled distance. They found that peak reflected pressure and impulse from a vertically-orientated cylinder (axis perpendicular to the span of the target) were much larger than those from a spherical mass or horizontally-orientated cylinder (up to a factor of 2.5). Furthermore, for large values of L/D it was observed that most of the energy was focused in the radial direction, whereas for small values of L/D most of the energy was focused in the axial direction. Similar findings are reported in the work of Sherkar et al. [19], Artero-Guerrero et al. [20], and Langran-Wheeler et al. [21, 22]. Pressure enhancements of between 3.0–6.6 have been reported in the literature for centrally-detonated [23], end-detonated [24], and double-end-detonated cylinders [25].

The aforementioned studies, and the empirical relations derived by Knock et al. [26, 27, 28], only consider pressure/impulse enhancement and spherical equivalence for a single point in free-air or on the target surface. Quantification of the influence of charge geometry on the deformation of blast loaded structures, however, requires knowledge of how the loading, and therefore spherical equivalence, is distributed across the entire loaded face of the target. Clutter and King [29] numerically investigated the response of blast containment chambers following internal detonation of spherical and non-spherical explosives. It was observed that the loading acting on the inside

of the chamber was higher magnitude and more non-uniform for the non-spherical charges, and the resulting peak plastic strain in the chamber wall was considerably larger.

Christian et al. [30] experimentally investigated the influence of charge shape on the response of steel-concrete composite panels. From the resulting panel damage/deformation, the authors estimated that the actual blast pressure generated by the 5 kg cylindrical charge ($L/D = 1/2$) was likely to be more than six times that of a spherical charge of the same mass. Chung Kim Yuen et al. [31] demonstrated that the deformation of blast loaded plates is highly sensitive to the orientation of squat ($L/D < 1$) cylindrical charges, again supporting the observation that smaller L/D charges focus more energy in the axial direction. In recent experimental work [32] it was observed that explosives formed into a $L/D = 1/3$ cylinder produced similar loading magnitudes and distributions to spherical explosives, and hence resulted in similar values of plate deformation, despite being placed a factor of three times further clear distance from the target.

Shi and Stewart [33] noted in 2015 that there were still no published equivalence values for scaled distances less than $1.24 \text{ m/kg}^{1/3}$, and stated “*further studies for explosions at small scaled distances are required to better quantify... the equivalent spherical mass ratio*” [33]. Since then, two notable studies have investigated the response of plates under the loading from cylindrical charges with a view to deriving near-field equivalence values and hence developing quick-running predictive methods. Nurick et al. [34] experimentally measured plate deformation following detonation of explosive charges of various mass and shape situated in close proximity to the target. Following this, the authors used ZND detonation theory to derive a series of effective explosive mass factors. It was shown that mid-point deflection was reasonably well correlated to effective mass, and therefore if two explosive shapes have identical effective mass, the resulting deflections will be similar. The concept of effective charge mass was later used by Davids et al. [35] to derive an empirical relationship between charge dimensions and the expansion of steel cylinders following internal detonation of cylindrical explosives.

Bortolan Neto et al. [36] aimed to develop a more accurate predictive approach by training an artificial neural network (ANN) using experimental data published by Jacob et al. [37]. Whilst the outputs from the network matched the experimental data (and supplementary validated numerical analyses used to increase the size of the training dataset) reasonably well, the predictive ability of the ANN was hampered by a lack of training data. Additionally, ANNs generally perform poorly when tasked with predicting outside the limits of the original training dataset. Whilst novel numerical techniques have been used to optimise plate geometries under blast loading [38,

39, 40, 41], the loading is typically represented using ConWep-type simplified load models and therefore only the effects of spherical explosives have been considered thus far.

There remains an opportunity, therefore, to derive spherical equivalence factors for near-field cylindrical explosives based on the consideration of plate deformation, in a manner that matches the simplicity of an analytical approach and the accuracy of a well-trained machine learning model or high-fidelity numerical scheme. This paper presents the development of such equivalence factors using a two-part validated numerical modelling approach using the LS-DYNA explicit solver [42].

Firstly, multi-material Arbitrary Lagrangian-Eulerian models are used to generate a suite of specific impulse distributions for cylinders of various aspect ratios at various scaled distances. These specific impulses are applied to Lagrangian plate models as initial velocity distributions, and it is shown that deformation can be readily predicted by transforming the loading into an equivalent uniform impulse, using the method proposed in Ref. [43] and explained in detail below. That is, peak displacement is shown to be strongly correlated to the initial kinetic energy uptake of the plates, and only knowledge of the imparted kinetic energy (derived from the specific impulse distribution) is required to transform a cylindrical charge into an equivalent sphere. Here, the equivalence factor is defined as $EF = W_S/W_C$, where W_S is spherical charge mass and W_C is cylindrical charge mass. $EF > 1$ therefore indicates when a cylinder will impart a larger kinetic energy compared to a sphere of equal mass. This forms the basis of the predictive method derived in the latter part of this paper, which is verified against an unseen numerical model to demonstrate the accuracy of the relations derived herein.

2. Theoretical framework

Experiments performed by Rigby et al. [32, 44] showed that the initial velocity profile of thin plates was directly proportional to the imparted specific impulse distribution, which was reasoned through consideration of local conservation of momentum. This work provided the underlying physical basis of the *energy equivalent uniform impulse* derived in Ref. [43]. An abridged derivation is presented here. Note that whilst analytical methods exist to quantify the effects of temporal and spatial variations of loading on dynamic plastic deformation [45, 46], such approaches typically require the spatial distribution of loading to be simplified (e.g. triangular, trapezoidal) and therefore may not be representative of the complex loading distributions from cylindrical charges. In this article, we follow the convention that thin plates are defined as those with central deflections that are several times greater

than plate thickness, and membrane strains that arise from transverse (out of plane) displacements are assumed to dominate [47]. This is applicable for plates with span:thickness > 20 [48].

Consider a collection of masses subjected to a distributed impulsive load, as in Figure 1(a). Each mass is connected to its neighbour by a fictitious lateral spring element. If these elements possess an *infinite* resistance to shear deformation, then each mass can instantaneously transfer load to its neighbours and the plate responds as a rigid body, as in Figure 1(b). The kinetic energy of the plate would therefore only be a function of the total impulse acting on the plate,

$$E_{k,l} = \frac{I^2}{2\rho t A} \quad (1)$$

where ρ and t are density and thickness of the plate, and I is total impulse, i.e. distributed specific impulse, i , integrated over the area of the plate, A . Since this results in a lower-bound estimate of kinetic energy, this term is given the subscript l .

Conversely, if the lateral spring elements possess *zero* resistance to shear, then the initial velocity profile of the plate would be directly proportional to the impulse distribution, as in Figure 1(c). The kinetic energy of each mass, and therefore the total kinetic energy of the plate, is dependent on the *distribution of specific impulse acting on the plate*,

$$E_{k,u} = \frac{1}{2\rho t} \int_A i^2 dA \quad (2)$$

Since this results in an upper-bound estimate of the kinetic energy, this term is given the subscript u . The experimental work in Refs. [32, 44] suggests that the initial kinetic energy uptake of a thin plate closely matches the upper-bound value.

The *energy equivalent uniform impulse*, I_{Ek} , is defined as the value of uniform impulse that, if applied to a plate, would result in the same kinetic energy uptake as the upper-bound kinetic energy associated with the distributed load,

$$I_{Ek} = \left(A \int_A i^2 dA \right)^{1/2} \quad (3)$$

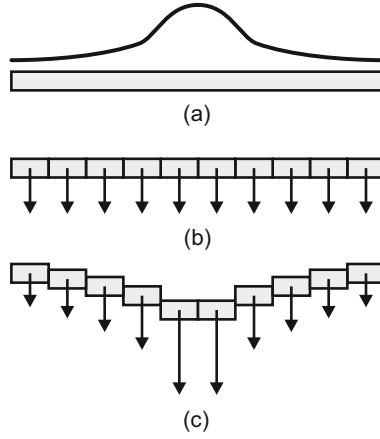


Figure 1: Initial distribution of specific impulse (a), and deformation modes associated with lower bound (b) and upper bound (c) kinetic energy, after [43]

Finally, the *impulse enhancement factor*, K_i , can be defined such that

$$I_{Ek} = K_i I. \quad (4)$$

This provides a quantitative measure of the non-uniformity of the applied load: $K_i = 1$ indicates a perfectly uniform load, and $K_i > 1$ indicates a load that is spatially non-uniform. Increasing values of K_i signify a loading distribution that is more concentrated with a greater difference between upper- and lower-bound kinetic energies. It can be said that total impulse, I , imparts the same momentum as the distributed load but a lower energy, whereas the energy equivalent impulse, I_{Ek} imparts the same kinetic energy as the distributed load but a higher momentum.

3. Numerical model validation

3.1. Overview

All numerical analyses were performed using LS-DYNA explicit solver [42], version 971 R8.10. Throughout this article a two-stage uncoupled analysis approach is adopted in order to study the response of plates under loading from various shapes of explosive detonated at various stand-off distances (SODs). Firstly, the detonation process, blast wave formation, and interaction of the blast wave with the target structure is modelled using an axi-symmetric, multi-material Arbitrary Lagrangian-Eulerian (MMALE) framework. The MMALE models are used to generate curves of specific impulse against radial ordinate (distance from the centre of the target), with

values of specific impulse calculated from numerical integration of the pressure histories at an array of tracer points located at 1 mm intervals along the reflecting surface. In the MMALE models, the reflecting surface is modelled using nodal-point constraints, i.e. it is effectively rigid, which implies that the response time of the structure is significantly longer than the loading duration and structural deformation remains zero throughout the duration of load application. The loading conditions are assumed to be perfectly impulsive and, as such, fluid-structure softening does not occur. The MMALE functionality in LS-DYNA has previously been validated against experimental blast loading data from spherical and cylindrical explosives [43, 49], hence this validation exercise focusses on comparison against previous experimental measurements of plate deformation only.

In the second part of the analysis, the plates are represented using Lagrangian shell elements, and the impulsive loading is applied directly as nodal-point velocities, v , through $v(x) = i(x)/\rho t$, where i , ρ and t are specific impulse, density and thickness of the plate as above, and x is radial ordinate. Whilst this technique has successfully been used to directly assign a known (experimentally measured) specific impulse distribution onto a plate in a Lagrangian-only analysis [43, 50, 51], it still remains to validate the MMALE/Lagrangian two-stage approach i.e. in situations when the loading is not known *a priori* and is instead determined through numerical analysis. The accuracy of this two-stage method is therefore demonstrated in this section by comparing the results against two sets of experimentally-measured plate deformation data.

In both sets of experiments, transient deformation was recorded at the centre of 3 mm thick, 300 mm diameter circular high-strength steel plates (Domex 355MC), clamped around the periphery. In the first set [32], two charge configurations were tested: 50 g PE4 spheres detonated at 44.0 mm clear distance to the target, and 50 g PE4 cylinders ($L/D = 1/3$), detonated at 145.0 mm clear distance to the target. In the second set [52], eight charge configurations were tested: 38 mm diameter PE4 cylinders with mass ranging from 10–25 g ($L/D = 0.14$ – 0.36) detonated at either 40 mm or 50 mm clear distance to the target.

3.2. Validation against Rigby et al. [32] data

3.2.1. MMALE model set up

The air was modelled using the *MAT_NULL material model and *EOS_LINEAR_POLYNOMIAL equation of state (EOS). The explosive was modelled using the *MAT_HIGH_EXPLOSIVE_BURN material model and Jones-Wilkins-Lee (JWL) semi-empirical equation of state, *EOS_JWL [53]. The material properties and EOS parameters for air and PE4 are given in Table 1. Since the composition of PE4 is nominally identical to that of C4 and it has been shown

to produce similar output [54], the EOS parameters for C4 published by Dobratz & Crawford [55] were used to represent the explosives in this study.

Table 1: Material model and equation of state parameters for air and PE4 [55]

MAT_NULL		
Parameter	Value	Unit
ρ_0	1.225	kg/m ³
EOS_LINEAR_POLYNOMIAL		
Parameter	Value	Unit
C_0	0.0	Pa
C_1	0.0	Pa
C_2	0.0	Pa
C_3	0.0	Pa
C_4	0.4	–
C_5	0.4	–
C_6	0.0	–
E_0	253.40E3	Pa
MAT_HIGH_EXPLOSIVE_BURN		
Parameter	Value	Unit
ρ_0	1601	kg/m ³
D	8193	m/s
P_{CJ}	28.00E9	Pa
EOS_JWL		
Parameter	Value	Unit
A	609.77E9	Pa
B	12.95E9	Pa
R_1	4.50	–
R_2	1.40	–
ω	0.25	–
E_0	9.00E9	Pa

Both MMALE validation models used a 250×250 mm domain of square axi-symmetric shell elements. The element side length in the spherical charge model equalled 1.25 mm and the element side length in the cylindrical charge model equalled 1.00 mm. An initial mesh sensitivity study was performed in Ref. [56] and determined that these element sizes were sufficient to achieve total impulse (specific impulse integrated over the central 100 mm radius region of the plate) to within 3% of the converged value, whilst still maintaining a reasonable analysis time (<10% the converged analysis time). Peak specific impulse and peak pressure values close to the axis of symmetry exhibited some mesh-dependent numerical ‘jetting’ [21], which renders such measures unsuitable for

mesh convergence studies (although total impulse is largely unaffected as this behaviour is extremely localised). The jetting effect can be minimised by avoiding an over-fine numerical mesh. The y -axis is automatically defined as the axis of symmetry, the top edge of the domain was constrained against normal translations to act as a rigid boundary, and the two remaining domain edges were set as ambient (outflow) boundaries.

The geometry of the explosives was defined using the `*INITIAL_VOLUME_FRACTION_GEOMETRY` keyword. Container type 6 (sphere) was used for the spherical charge model, defining a 19.5 mm radius sphere centred on the axis of symmetry, 63.5 mm vertical distance from the reflecting boundary (44.0 mm clear distance). Container type 5 (rectangular box) was used for the cylindrical charge model, with one corner located on the axis of symmetry, 145 mm vertical distance from the reflecting boundary, and the opposite corner located 24.5 mm horizontal distance from the axis of symmetry and 161.5 mm vertical distance from the reflecting boundary, see Figure 2. The detonators were not explicitly modelled and instead the explosives were point-detonated in the centre using the `*INITIAL_DETONATION` keyword.

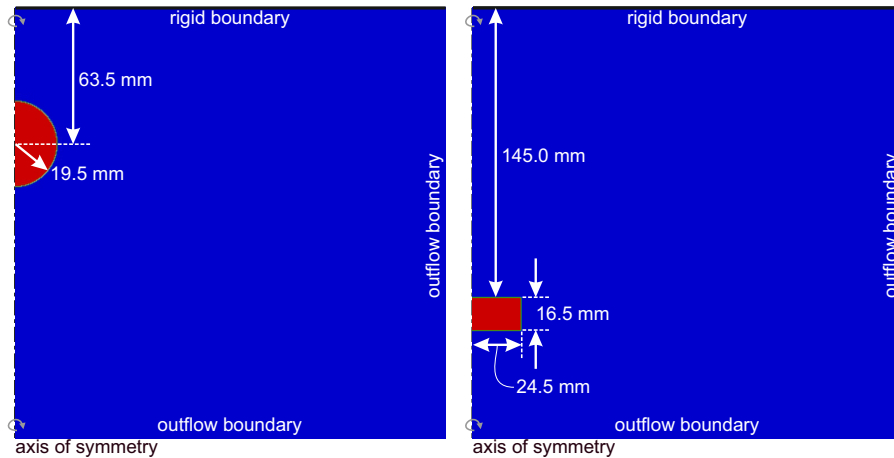


Figure 2: Geometry of the spherical [left] and cylindrical [right] MMALE validation models

3.2.2. Lagrangian modelling set up

The specific impulse distributions determined from the spherical and cylindrical charge models were used as input loading for the second stage models. In the experimental work in Rigby et al. [32], digital image correlation (DIC) was used to measure transient deformation of the 300 mm diameter, 3 mm thick Domex 355MC plates,

fully clamped around the perimeter, subjected to the blast loading from spherical and cylindrical PE4 explosives as outlined previously. Transient displacement data were recorded in six tests; three for each charge configuration.

The plates were modelled in quarter-symmetry as 200×200 mm square plates. Any nodes with radial ordinate ≥ 150 mm were constrained against all translations and rotations to match the experimental support conditions. Nodes along the symmetry planes were constrained appropriately. The plates were meshed with 2×2 mm, 4-noded fully integrated quadrilateral shell elements with 3 mm thickness and five through-thickness integration points to be consistent with previous studies [43, 57]. The simplified Johnson-Cook material model [58] was used (*MAT_SIMPLIFIED_JOHNSON_COOK), with parameters for Domex 355MC steel as determined in Ref. [59] and shown in Table 2. The MMALE specific impulse distributions from the part one analyses were applied to the plates using the *INITIAL_VELOCITY_NODE keyword according to the methodology outlined in Ref. [43].

Table 2: Johnson-Cook material properties for Domex 355MC steel [59]

*MAT_SIMPLIFIED_JOHNSON_COOK		
Parameter	Value	Unit
ρ	7830	kg/m ³
E	206.8E9	Pa
ν	0.30	–
A	362E6	Pa
B	642E6	Pa
n	0.5597	–
C	0.032	–

3.2.3. Results

Figure 3 shows experimental and numerical plate deformations for spherical (a) and cylindrical (b) charge models. The numerical peak deflections (spheres: 17.97 mm, cylinders: 22.49 mm) compare well with the mean experimental peak deflections (spheres: 20.54 mm, cylinders: 21.96 mm), as do the general forms of the deflection histories. Whilst cylindrical specific impulse distributions have been shown to slightly over-predict loading at the plate centre [43], this results in a relatively modest over-prediction of plate deformation ($\sim 3\%$) on account of the small area of the plate for which specific impulses are over-predicted and therefore its minimal contribution to kinetic energy/equivalent uniform impulse.

Furthermore, the results are also in good agreement with those presented in Ref. [43] for fully-coupled MMALE analyses (spheres: 20.00 mm, cylinders: 21.69 mm) and Lagrangian-only models under experimentally-measured specific impulse distributions (spheres: 20.52 mm, cylinders: 21.83 mm), giving additional confidence in the

two-stage approach adopted in this article. It is worth noting that, in total, the analysis time of the fully-coupled MMALE models in Ref. [43] is approximately a factor of 10–15 greater than the analysis time of the two-stage models presented herein (~20 hours compared to ~90–120 minutes).

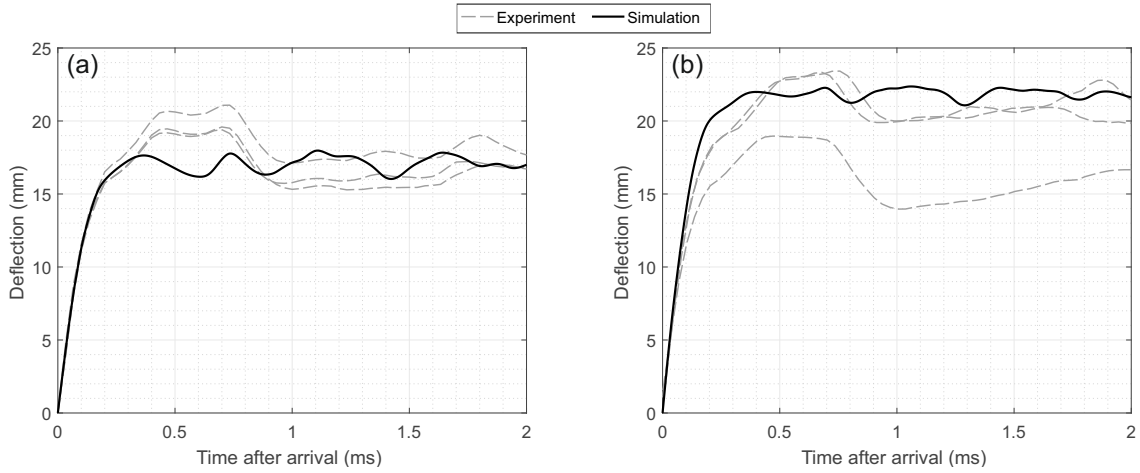


Figure 3: Validation of numerical deformation of 300 mm diameter, fully clamped, 3 mm thick steel plates against experimental data from Ref. [32]: a) 50 g sphere at 44.0 mm clear SOD; b) 50 g ($L/D = 1/3$) cylinder at 145.0 mm clear SOD

3.3. Validation against Curry & Langdon [52] data

3.3.1. Model set up

The MMALE model set up was identical to the previous validation study, i.e. the air and explosive were modelled using `*MAT_NULL`, `*EOS_LINEAR_POLYNOMIAL`, `*MAT_HIGH_EXPLOSIVE_BURN`, and `*EOS_JWL` respectively, as in Table 1. Again, a 250×250 mm domain of 1 mm square MMALE axi-symmetric shell elements was used, with the explosive geometry defined using the `*INITIAL_VOLUME_FRACTION_GEOMETRY` keyword. Container type 5 (rectangular box) was used to specify the rectangular shape of the charge (cylindrical when rotated around the symmetry axis) with one corner located on the axis of symmetry, at either 40 mm or 50 mm vertical distance from the reflecting boundary, and the opposite corner located 19.0 mm horizontal distance from the axis of symmetry and 5.5–13.8 mm from the front face (nearest the target) of the explosive, see Table 3. The explosives were point-detonated in the centre of the back face as per the experimental work [52] using the `*INITIAL_DETONATION` keyword.

Specific impulse distributions from the first stage analysis were mapped onto the second stage models using the `*INITIAL_VELOCITY_NODE` keyword as previously. The quarter-symmetric 200×200 mm square plates (2×2 mm, 4-

noded fully integrated quadrilateral shell elements, 3 mm thickness, five through-thickness integration points) were fully constrained at any distance ≥ 150 mm from the plate centre to match the experimental support conditions. The platers were made of Domex 355MC steel (Table 2).

Whilst DIC was also used to measure transient deformation in the experimental work in Curry & Langdon [52], only peak deflection is used here to validate the two-stage numerical modelling approach.

3.3.2. Results

Peak deflections from the experiments [52] and numerical analyses are given in Table 3. Figure 4 shows experimental and numerical peak deflection as a function of charge mass for the two clear SODs, and Figure 5 shows the agreement between experimental and numerical results, where a straight line of unit gradient indicates a perfect fit.

Table 3: Input parameters and results from validation against Curry & Langdon [52] experiments

W (g)	L/D (-)	L (mm)	D (mm)	Clear SOD (mm)	Z (m/kg ^{1/3})	t (mm)	Peak deflection (mm)		
							Exp.	Num.	% diff.
10	0.14	5.5	38	40	0.198	3	22.02	19.85	-9.8
15	0.22	8.3	38	40	0.179	3	25.28	25.99	2.8
20	0.29	11.0	38	40	0.168	3	30.67 [†]	31.05	1.2
25	0.36	13.8	38	40	0.160	3	36.27	35.02	-3.5
10	0.14	5.5	38	50	0.245	3	16.84	17.94	6.5
15	0.22	8.3	38	50	0.219	3	21.74	23.35	7.4
20	0.29	11.0	38	50	0.204	3	24.66 [*]	27.92	13.5
25	0.36	13.8	38	50	0.195	3	30.46	31.38	3.0

*Average of two tests

†Average of three tests

The numerical results are typically within +/-10% of the experimental peak deflections, with the exception of one of the 20 g, 50 mm SOD tests which is over-predicted by approximately 5 mm. It is worth noting that the peak deflection from this test appears lower than the general trend observed in Figure 4, and this over-prediction is therefore not indicative of a systemic error in the modelling approach. The remaining 50 mm SOD tests are slightly over-predicted by approximately 1–2 mm in each case, with an average deviation of +8%. The numerical simulations are in slightly better agreement with the 40 mm SOD tests, with a maximum under-prediction of approximately 2 mm and an average deviation of -2%. It can be concluded that the two-stage MMALE/Lagrangian analysis method adopted in this article has demonstrated a sufficiently high level of accuracy and can therefore be

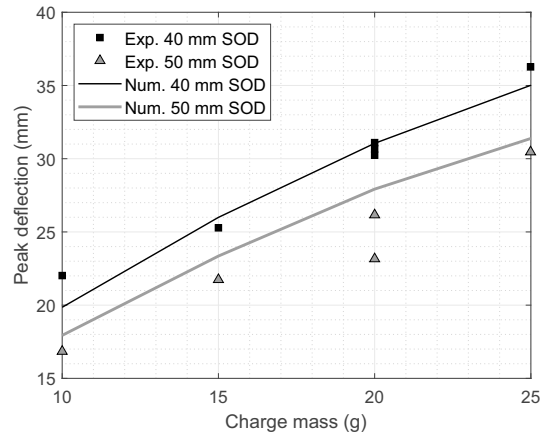


Figure 4: Peak deflection versus charge mass for 40 mm and 50 mm clear SOD experiments [52] and numerical analyses

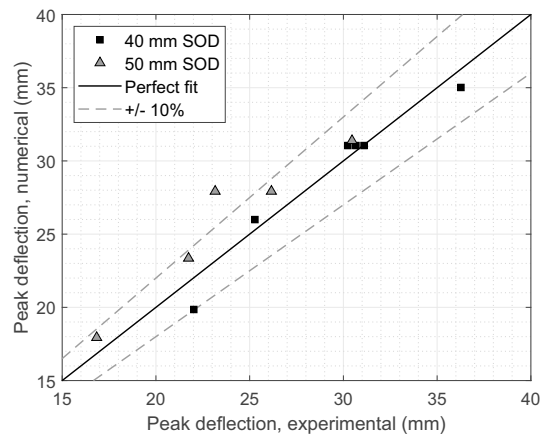


Figure 5: Numerical versus experimental [52] peak deflection, with perfect fit and +/-10% bounds shown

used with confidence to model plate deformation under blast loading from near-field cylindrical charges of varying L/D .

4. Parametric study

4.1. Design and compiled results

A detailed parametric study was conducted in order to quantify the loading distribution, and to assess subsequent plate deformation, from a range of spherical and cylindrical explosive charges. Since impulse enhancement

factor, i.e. the ratio between the energy equivalent and total impulse, is invariant of plate density and thickness [60], these were retained from the validation exercise. The plate dimensions were extended to 400×400 mm square (modelled as a 200×200 mm square in quarter symmetry), fully clamped around the perimeter, to enable a greater combination of impulse and energy equivalent impulse to be studied. The influence of plate dimensions on spherical charge equivalence will be considered later in this article.

The remaining parameters governing specific impulse distribution, for a given charge mass, are: charge shape; cylinder aspect ratio (L/D), and; stand-off distance (SOD, hereafter denoting distance from the target to the *centre* of the charge). A consistent charge mass of 100 g PE4 was used throughout, with variations in SOD providing a range of scaled distances. Again, the explosives were point detonated in the centre. Relevant input parameters are summarised in Table 4. For the $L/D = 5$ cylinder, analyses at SOD = 0.050 m and 0.225 m were omitted to avoid simulations where the explosive overlapped the edges of the domain.

Table 4: Parametric study inputs

Shape	L/D (-)	W (kg)	L (mm)	D (mm)	SOD (m)	Z ($\text{m}/\text{kg}^{1/3}$)	t (mm)
Sph.	-	0.1	-	49.2	0.050–0.225	0.162–0.431	3
Cyl.	0.20	0.1	14.7	73.5	0.050–0.225	0.108–0.485	3
Cyl.	0.33	0.1	20.7	62.0	0.050–0.225	0.108–0.485	3
Cyl.	1.00	0.1	43.0	43.0	0.050–0.225	0.108–0.485	3
Cyl.	3.00	0.1	89.5	29.8	0.050–0.225	0.108–0.485	3
Cyl.	5.00	0.1	125.7	25.1	0.075–0.200	0.162–0.485	3

For each charge configuration, four models were run:

1. Axi-symmetric air blast MMALE analysis to determine specific impulse distribution along the target face
2. ‘Distributed’: quarter-symmetric Lagrangian plate under the unmodified peak specific impulse distribution from the MMALE model
3. ‘Uniform’: quarter-symmetric Lagrangian plate under the total impulse from the MMALE model applied as a uniformly distributed load
4. ‘Equivalent’: quarter-symmetric Lagrangian plate under the energy equivalent impulse (calculated using Equation 3 and the distributed impulse from the MMALE model) applied as a uniformly distributed load

The loading in the Lagrangian models was applied as an impulsive load using initial nodal velocities as previously. In total, 46 different charge configurations were considered, resulting in 46 MMALE models and 138 Lagrangian models, and therefore 184 simulations in total. A detailed compilation of the results from the parametric study is provided in Table 5.

Nurick and Martin [61] define the damage number, ϕ , as:

$$\phi = \frac{I_{Ek}}{2t^2 \sqrt{L_A L_B} \rho \sigma_0} \quad (5)$$

where I_{Ek} , t , and ρ are energy equivalent impulse, plate thickness, and density as previously, L_A and L_B are plate length and breadth ($L_A = L_B = 0.4$ m), and σ_0 is static yield stress (362 MPa). Partial tearing around the plate boundary was observed for quadrangular plates when $\phi \gtrsim 28$ in [61]. The $L/D = 1/5$ cylinder at both 0.05 m and 0.075 m SOD, and the $L/D = 1/3$ cylinder at 0.05 m SOD resulted in $\phi > 28$ and therefore their deflections have been omitted from Table 5. The specific impulse distributions for these cases, however, have been retained to facilitate development of the equivalence factors in the next section since the loading is assumed to be perfectly impulsive throughout and development of specific impulse on the loaded face is independent of plate response and thickness.

4.2. Influence of L/D on loading and deflection

A number of observations can be made on how loading and deformation are influenced by aspect ratio. Figure 6 shows the influence of aspect ratio on specific impulse distribution, as determined from the MMALE analyses for 100 g cylinders at 100 mm SOD. Here, total and energy equivalent impulse (I and I_{Ek}) range from 141.3 N.s and 350.6 N.s ($K_i = 2.48$) for $L/D = 1/5$, to 36.9 N.s and 67.5 N.s ($K_i = 1.83$) for $L/D = 5$: a factor of ~ 4 difference in impulse and a factor of ~ 5 difference in energy equivalent impulse due to changes in aspect ratio alone. This is in broad agreement with the findings in Ref. [18], i.e. decreasing axial loading component and increasing radial loading component as L/D increases.

For comparison, the total and energy equivalent impulse for a 100 g sphere at 100 mm are 91.3 N.s and 120.2 N.s respectively ($K_i = 1.32$). It is evident that some degree of axial focussing occurs even for high values of L/D : the epicentral peak specific impulse for the $L/D = 5$ cylinder is 6.56 MPa.ms; a factor of 2.5 greater than the epicentral peak specific impulse from the spherical charge (2.67 MPa.ms). Throughout, the cylindrical peak

Table 5: Parametric study results

Shape	L/D (-)	SOD (m)	Impulse (N.s)		Deflection (mm)		
			Total	Energy equivalent	Distributed	Uniform	Equivalent
Sph.	-	0.050	101.3	211.8	101.3	45.9	107.3
Sph.	-	0.075	97.7	152.9	74.7	43.9	73.8
Sph.	-	0.100	91.3	120.2	57.8	40.5	56.4
Sph.	-	0.125	85.5	100.8	47.8	37.5	45.7
Sph.	-	0.150	80.4	88.4	41.8	34.8	39.0
Sph.	-	0.175	75.4	79.5	36.8	32.3	34.4
Sph.	-	0.200	70.0	72.2	33.0	29.6	30.8
Sph.	-	0.225	63.5	65.3	29.5	27.0	27.7
Cyl.	0.20	0.050	152.0	508.5	-	-	-
Cyl.	0.20	0.075	147.3	421.5	-	-	-
Cyl.	0.20	0.100	141.3	350.6	171.1	67.8	180.2
Cyl.	0.20	0.125	137.3	299.0	146.2	65.7	157.4
Cyl.	0.20	0.150	133.2	262.3	131.1	63.5	139.3
Cyl.	0.20	0.175	127.3	234.4	117.9	60.3	122.4
Cyl.	0.20	0.200	121.6	212.6	106.9	57.1	107.8
Cyl.	0.20	0.225	118.5	196.5	98.8	55.5	97.6
Cyl.	0.33	0.050	134.7	462.7	-	-	-
Cyl.	0.33	0.075	130.7	372.6	181.7	62.2	190.2
Cyl.	0.33	0.100	125.0	303.6	147.1	59.0	159.4
Cyl.	0.33	0.125	120.9	254.5	122.8	56.7	135.0
Cyl.	0.33	0.150	117.3	220.2	108.1	54.8	112.8
Cyl.	0.33	0.175	111.8	194.8	96.3	51.7	96.7
Cyl.	0.33	0.200	107.1	176.1	87.0	49.1	86.2
Cyl.	0.33	0.225	103.1	161.5	79.4	46.9	78.3
Cyl.	1.00	0.050	86.8	280.3	135.2	38.2	148.5
Cyl.	1.00	0.075	83.7	213.1	100.5	36.5	108.1
Cyl.	1.00	0.100	80.6	169.1	79.2	34.9	82.3
Cyl.	1.00	0.125	76.4	139.2	64.9	32.9	66.7
Cyl.	1.00	0.150	73.8	119.7	56.0	31.6	56.1
Cyl.	1.00	0.175	71.6	107.2	49.9	30.5	49.2
Cyl.	1.00	0.200	65.3	96.9	44.4	27.7	43.5
Cyl.	1.00	0.225	60.7	89.4	40.6	25.8	39.5
Cyl.	3.00	0.050	48.1	186.5	88.0	20.8	92.0
Cyl.	3.00	0.075	45.5	113.7	51.5	19.8	52.8
Cyl.	3.00	0.100	42.2	89.9	40.9	18.5	39.8
Cyl.	3.00	0.125	41.7	72.6	33.3	18.3	31.0
Cyl.	3.00	0.150	38.4	61.3	27.9	17.1	26.1
Cyl.	3.00	0.175	36.5	55.0	24.7	16.3	23.5
Cyl.	3.00	0.200	34.8	51.6	22.7	15.7	22.2
Cyl.	3.00	0.225	33.6	50.3	22.0	15.3	21.7
Cyl.	5.00	0.075	37.1	102.2	47.4	16.6	46.4
Cyl.	5.00	0.100	36.9	67.5	31.3	16.5	28.6
Cyl.	5.00	0.125	34.3	56.8 ¹⁷	26.7	15.6	24.2
Cyl.	5.00	0.150	32.4	47.5	22.1	14.9	20.6
Cyl.	5.00	0.175	30.7	41.9	19.1	14.3	18.4
Cyl.	5.00	0.200	29.1	39.3	17.8	13.8	17.4

specific impulses possess a higher epicentral value than the spherical charge loading, with the area over which the cylindrical loading exceeds the spherical loading approximately inversely proportional to L/D . It is likely, therefore, that spherical equivalence will be dependent on the dimensions of the target, with smaller targets more sensitive to, and therefore exhibiting larger enhancement factors on account of, this central focussing.

The relationship between L/D and peak deflection is examined in Figure 7 for SOD = 100 mm. Here, the effect of a more concentrated specific impulse distribution can be clearly seen: for $L/D = 1$, the total impulse is 80.6 N.s, yet the peak deflection (79.2 mm) exceeds the deformation of the plate under the spherical load (57.8 mm), despite the spherical impulse being larger (91.3 N.s). The energy equivalent uniform impulse values are 169.1 N.s and 120.2 N.s for the cylindrical and spherical charge respectively, suggesting that plate deflection is more strongly dependent on energy equivalent rather than total impulse.

Deflection under the cylindrical loading is equal to deflection under the spherical loading at approximately $L/D = 1.5$ – 1.8 . This suggests that for this aspect ratio, target size (0.4×0.4 m, scaled target size 0.86×0.86 m/kg^{1/3}) and scaled distance (0.215 m/kg^{1/3}), the equivalence factor is 1.0.

4.3. Verification of energy equivalent uniform impulse and kinetic energy uptake

In this study, plate deflection was analysed under three types of loading as explained previously: the distributed load and two forms of uniform load which conserve either momentum (total impulse) or kinetic energy (energy equivalent impulse). The results in Table 5 show that, for each loading model, there is a high level of agreement between the peak deflection under distributed and energy-conserved equivalent loading, I_{Ek} . Here, the mean absolute relative difference between the two models is 4.3%, and all models are within 10% (maximum relative error of 9.98% for $L/D = 1/3$ and SOD = 0.125 m). There appears to be no strong correlation between the agreement attained and the magnitude of energy equivalent impulse (weak positive correlation, coefficient of determination $R^2 = 0.049$) or the impulse enhancement factor (weak positive correlation, coefficient of determination $R^2 = 0.051$).

This suggests that peak plate deflection under an energy equivalent uniform load, derived by conserving and equating kinetic energy uptake from the distributed load, will be similar to peak plate deflection under the distributed load. Whilst not the primary aim of this article, this transformation is highly advantageous in that it enables a complex spatially-varying load to be expressed as a single parameter (energy equivalent impulse per unit area) which can be used as an input variable in simple well-established engineering models e.g. the SDoF method

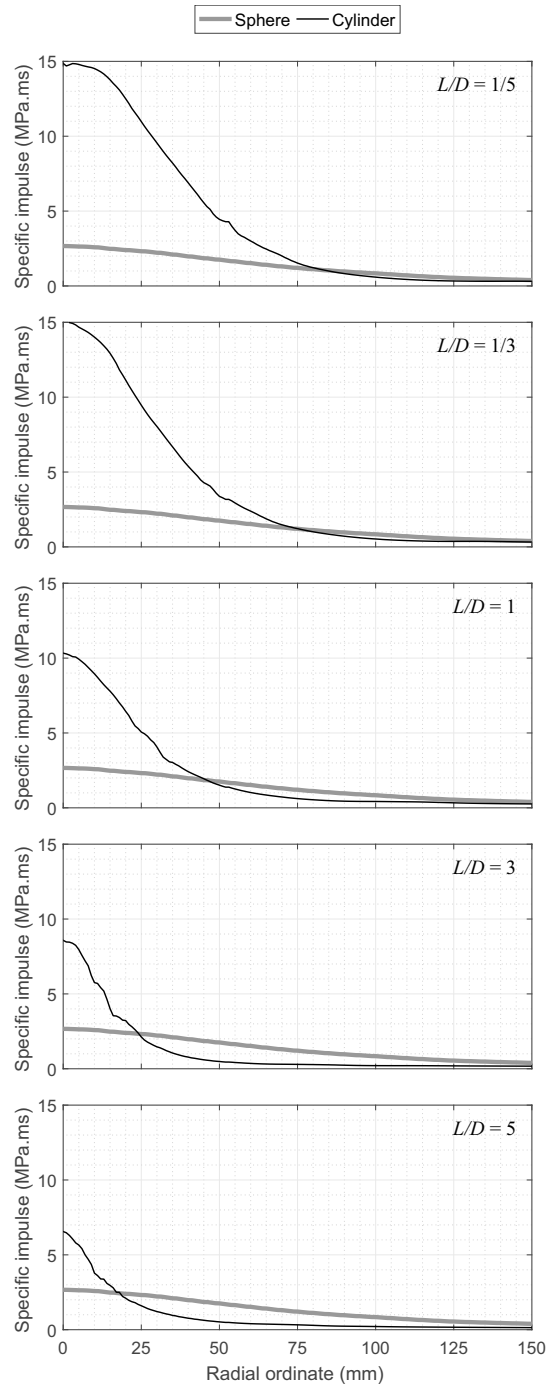


Figure 6: Example specific impulse distributions from MMALE analyses for 100 g cylinders and sphere at 100 mm SOD

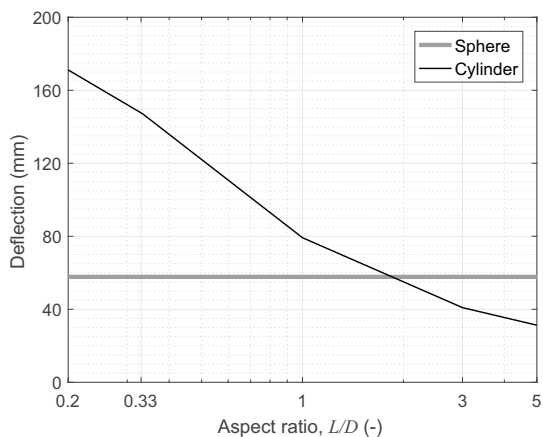


Figure 7: Plate deflection versus aspect ratio (L/D) for 100 g cylinders and sphere at 100 mm SOD

[62] or the empirical laws derived in Ref. [61] for prediction of large inelastic deformation of plates under uniform impulsive loading. Agreement between peak deflection under distributed and momentum-conserved uniform loading, I , is considerably less good, with a mean absolute relative error of 43% and a maximum relative error of 76%.

Figure 8 shows deformation profiles (deflected shape at the moment of peak deflection) and deflection-time histories at the centre of the plates for $L/D = 1$ cylinders at 100 mm (a, b), 150 mm (c, d) and 200 mm (e, f) SOD. It can be seen that whilst there are differences in the deformed profile of the plates under the distributed and equivalent loading, the midspan (peak) deflection values are in close agreement, as previously discussed. Since the distributed and energy equivalent loading imparts the same kinetic energy, these deformation profiles therefore represent different distributions of the same total strain energy. This strain energy localisation may become significant during fracture and/or failure, however the transformation is satisfactory in this study on account of the near-identical peak deflections.

Whilst further work is required to quantify the limits of validity of the approach detailed in this article, it is known that partial tearing is observed for quadrangular plates when $\phi \gtrsim 28$ and hence this damage number should serve as an initial upper limit. Since the equivalence factor is governed by Z , L/D , and span only, the derived equivalence is invariant of the properties of the plate itself. For a particular loading distribution and spherical equivalence, certain plates will fail (in which case the transformation is not valid), and certain plates will only

deform plastically (in which case the transformation is valid). The validity of this approach is therefore not limited to a range of equivalence factors.

Additionally, the rapid rise to peak deflection observed for plates under the distributed loading model may be significant for materials more sensitive to strain rate effects. Again, however, the effects appear minimal for the plates considered in this study.

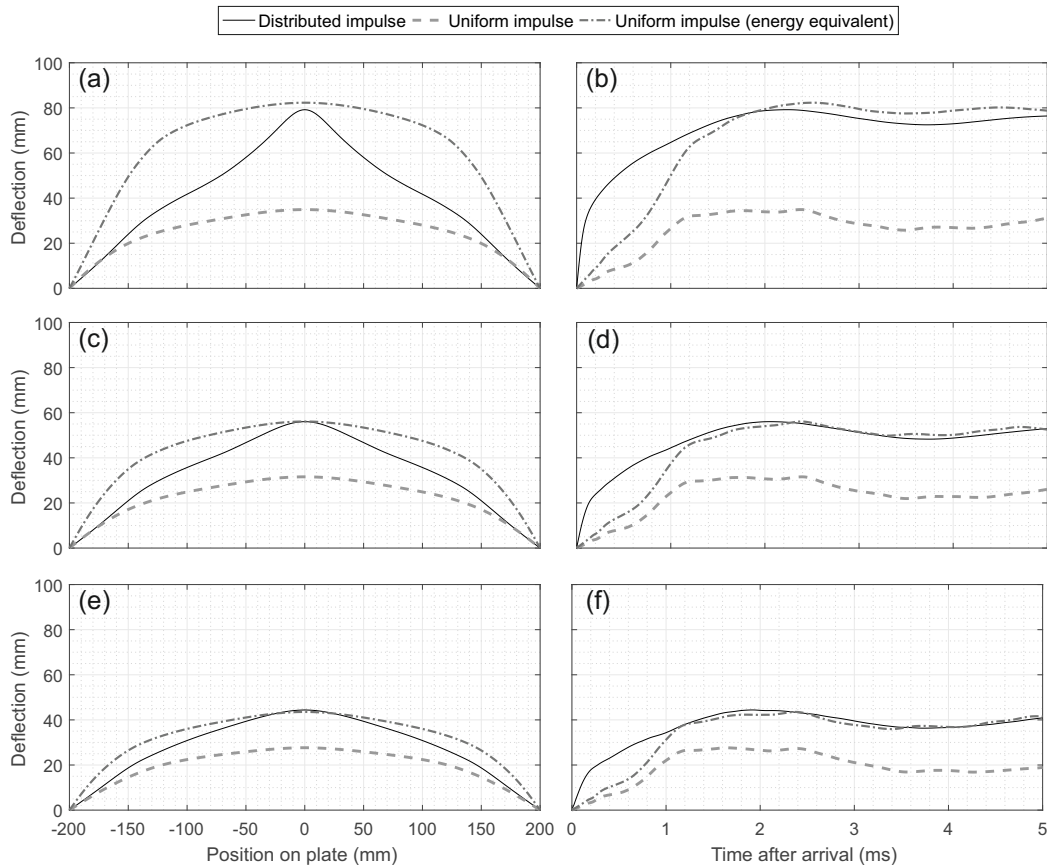


Figure 8: Deflection of 400 mm square clamped plates under distributed, uniform, and energy equivalent uniform impulses: (a) peak deformation profile at maximum deflection, 100 g $L/D = 1$ cylinder at 100 mm; (b) deflection-time history, 100 g $L/D = 1$ cylinder at 100 mm; (c) peak deformation profile at maximum deflection, 100 g $L/D = 1$ cylinder at 150 mm; (d) deflection-time history, 100 g $L/D = 1$ cylinder at 150 mm; (e) peak deformation profile at maximum deflection, 100 g $L/D = 1$ cylinder at 200 mm; (f) deflection-time history, 100 g $L/D = 1$ cylinder at 200 mm

The results have clearly demonstrated that peak displacement is strongly correlated to the initial kinetic energy uptake of the plates, and that distributed *and* energy-equivalent uniform loads will result in a similar peak deflection, albeit with a different deformed profile. That is, kinetic energy uptake is the key parameter governing

plate deformation. In Figure 9, total uniform impulse and energy equivalent uniform impulse (integrated over plate area) are plotted against peak deflection under the distributed load. A strong linearity exists between equivalent impulse and deflection (coefficient of determination $R^2 = 0.998$), with a small negative offset due to increasing contribution of bending behaviour, relative to membrane action, for smaller values of impulse and deflection [63]. Referring back to Figure 8, it is evident that this linearity is invariant of the *shape* of the loading distribution, only the *magnitude* of kinetic energy uptake and energy equivalent impulse.

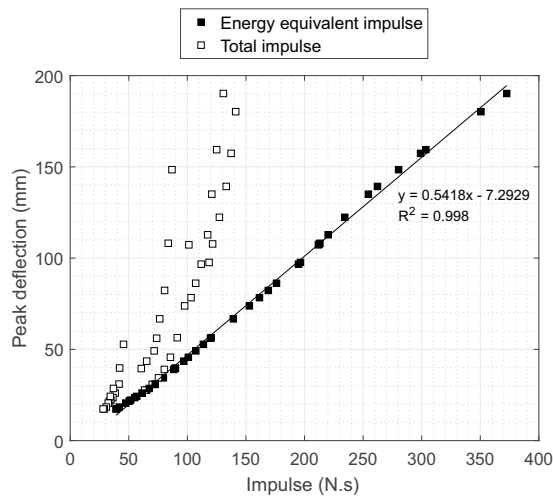


Figure 9: Linear relationship between energy equivalent impulse and deflection for all models

It can be concluded, therefore, that if two different explosives produce different distributions but the same kinetic energy uptake and therefore energy equivalent impulse, they will result in the same central peak deflection. Results in the parametric study demonstrate that this approach is valid for uniform loads and for distributed loads with values of impulse enhancement factor up to at least 3.87 (that is, where the distributed loading imparts 3.87 times more kinetic energy than the momentum-conserved total impulse). It is now possible to calculate the kinetic energy uptake after loading from a cylindrical explosive with the range $0.2 \leq L/D \leq 5$ and $0.108 \leq Z \leq 0.485$, and calculate the mass of a sphere such that, when detonated at the same SOD, will impart the same kinetic energy and thus result in the same deflection (for centrally detonated charges). This approach is adopted in the following section to derive equivalence factors, $EF = W_S/W_C$, where W_S is spherical charge mass and W_C is cylindrical charge mass. Hopkinson-Cranz scaling [64, 65] is used to express the results in terms of a unit cylindrical mass.

5. Spherical equivalence of cylindrical explosives

5.1. Development of equivalence factors

In order to derive equivalence factors for a wide range of Z and L/D , specific impulse distributions from the previous cylindrical MMALE simulations were expressed in scaled terms, i.e. as the resultant load from a unit mass of explosives throughout. This was achieved by multiplying distances and specific impulses by $(1/0.1)^{1/3} = 2.15$ according to Hopkinson-Cranz scaling [64, 65], where 0.1 kg is the charge mass used in the previous simulations. Since the cylindrical models are unit mass, distance and scaled distance can be used interchangeably.

These scaled loading distributions were mapped onto a grid of 0.5×0.5 mm elements for target sizes of 0.25×0.25 m, 0.50×0.50 m and 1.00×1.00 m in order to evaluate spherical equivalence factors for a range of scaled target dimensions. The original MMALE analyses reported specific impulses out to $0.86 \text{ m/kg}^{1/3}$ from the target centre, so extrapolation was used for the small number of grid points outside of this region. To facilitate this, a value of $i = 0$ was appended to each distribution, at an arbitrary large distance from the plate centre, such that the specific impulse distributions remained monotonically decreasing and positive beyond $0.86 \text{ m/kg}^{1/3}$ from the target centre.

The previously-determined spherical MMALE specific impulse distributions were expressed at a range of charge masses/scales by multiplying distances and specific impulses by $(W_S/0.1)^{1/3}$, where W_S is the spherical mass at the scale that the results are being expressed at, and 0.1 kg is the charge mass used in the previous simulations. As with the cylindrical distributions, these were mapped onto a grid of 0.5×0.5 mm elements for target sizes of 0.25×0.25 m, 0.50×0.50 m and 1.00×1.00 m.

The kinetic energy uptake was calculated for each specific impulse distribution according to Equation 3, over the entire range of charge shapes (spherical and cylindrical: $0.2 \leq L/D \leq 5$), charge masses (unit for cylinders, $0.4 \leq W_S \leq 10$ kg for spheres), scaled distances ($0.108 \leq Z \leq 0.485 \text{ m/kg}^{1/3}$ when scaled off the cylindrical charge mass), and scaled target sizes ($0.25, 0.50$ and $1.00 \text{ m/kg}^{1/3}$ when scaled off the cylindrical charge mass). In total, kinetic energy uptake was calculated for 168 cylindrical charge configurations and 2,592 spherical charge configurations ($9 \times \text{SODs}$, $96 \times \text{Ws}$, and 3 target sizes).

Once kinetic energy uptake was evaluated for each cylindrical charge, logarithmic interpolation was used to determine the spherical mass, W_S , required to result in the same value of $E_{k,u}$ for the same SOD and target size. Since $W_C = 1$ throughout, the spherical mass required to achieve the same kinetic energy uptake would, by

definition, equal the spherical enhancement factor, EF.

Figure 10 shows contours of spherical equivalence for the range of parameters studied. As expected, EF is dependent on aspect ratio, with smaller values of L/D yielding larger values of EF. To a lesser extent, EF is also dependent on scaled distance, with the largest values of EF found for larger values of Z and smaller values of L/D . This is due to differences in the rate of decay of peak specific impulse with respect to scaled distance and should be viewed as a measure of the relative weakness of the spherical charge loading, rather than the relative strength of the cylindrical charge loading at these scaled distances. For example, at $Z = 0.485 \text{ m/kg}^{1/3}$, the normally reflected peak specific impulse is $2.51 \text{ MPa.ms/kg}^{1/3}$ for the spherical charge and $14.1 \text{ MPa.ms/kg}^{1/3}$ for the cylindrical charge, compared to $19.6 \text{ MPa.ms/kg}^{1/3}$ and $56.7 \text{ MPa.ms/kg}^{1/3}$ for the spherical and cylindrical charge respectively at $Z = 0.108 \text{ m/kg}^{1/3}$. Clearly, $Z = 0.108 \text{ m/kg}^{1/3}$ still represents a worst-case scenario in terms of loading and deformation, despite EF not exceeding ~ 2 for all target sizes.

Finally, EF appears to also be dependent on scaled target size, with smaller target sizes generally yielding larger values of EF. This is on account of the high epicentral focussing of the cylindrical charge impulse (see Figure 6): the smaller the area, the greater the apparent disparity between the cylindrical and spherical specific impulse distributions, and hence the larger spherical mass required to achieve equivalence and the larger value of EF for a given Z and L/D .

5.2. Verification of equivalence factors

In order to demonstrate the accuracy of the derived equivalence factors, three verification examples were performed using the following inputs (see Figure 10):

- (i) $L/D = 1.30$, $EF = 1.00$ and $t = 8.0 \text{ mm}$
- (ii) $L/D = 0.80$, $EF = 1.60$ and $t = 10.0 \text{ mm}$
- (iii) $L/D = 0.60$, $EF = 2.00$ and $t = 12.5 \text{ mm}$

In all examples, scaled distance and scaled target size were set as $0.220 \text{ m/kg}^{1/3}$ and $0.50 \times 0.50 \text{ m/kg}^{1/3}$ respectively. These parameters did not form part of the original parameter study and can be considered to represent unseen combinations of Z and L/D . In all examples the charge mass was set as $W_C = 0.512 \text{ kg}$. As in the parametric study, the modelling was performed in two parts: MMALE analyses were first used to establish specific

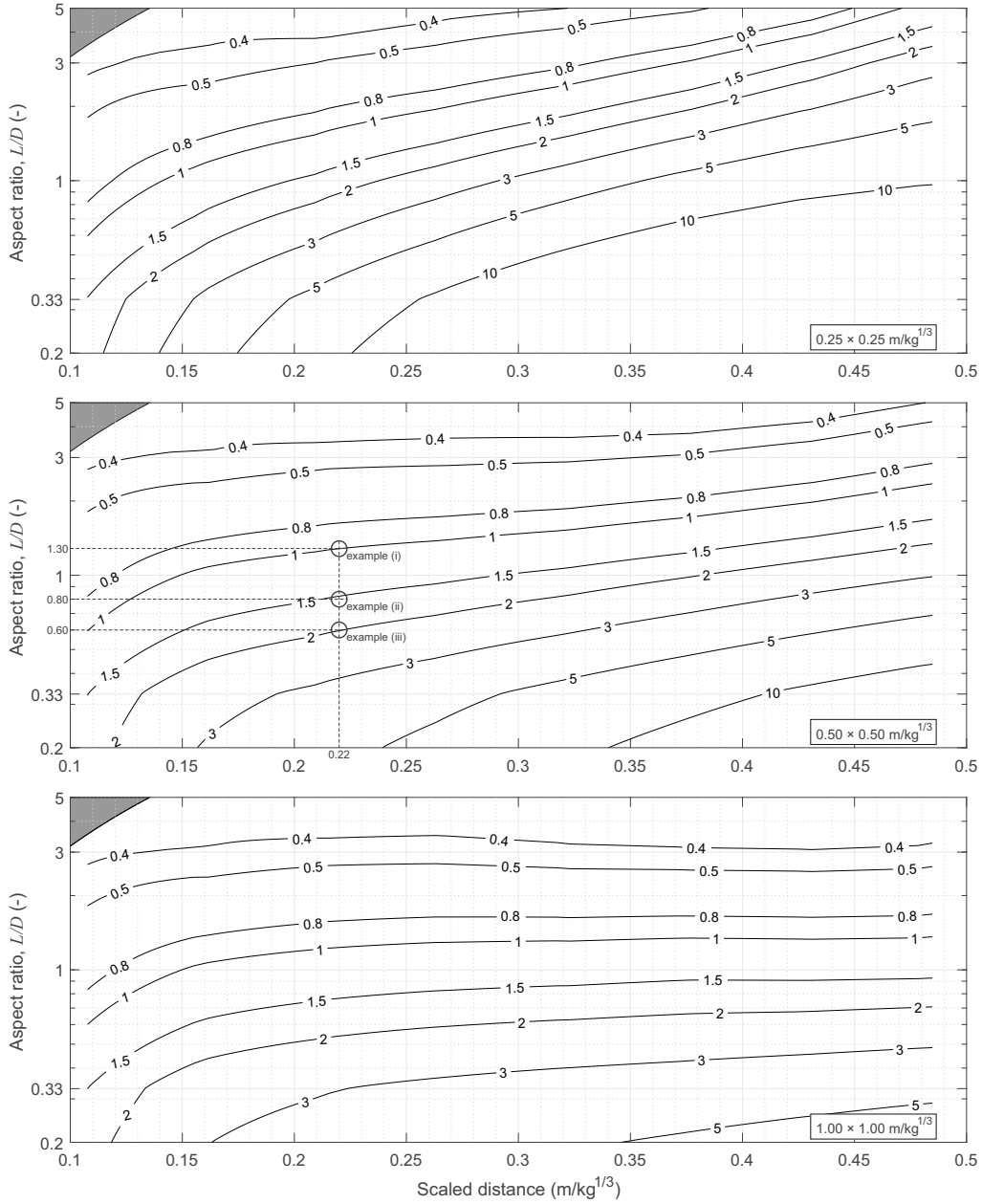


Figure 10: Contours of spherical charge equivalence factor ($EF = W_S/W_C$) as a function of aspect ratio and scaled distance, for square targets with scaled dimensions of $0.25 \times 0.25 \text{ m/kg}^{1/3}$, $0.50 \times 0.50 \text{ m/kg}^{1/3}$, and $1.00 \times 1.00 \text{ m/kg}^{1/3}$ respectively (scaled according to W_C). Verification examples described in Section 5.2 are marked by the grey circles. Note: small shaded region in the top-left of each plot indicates where $L/2 < \text{SOD}$

impulse distributions from the different charge configurations (one cylinder and three spheres per example, see Table 6), and subsequent Lagrangian analyses simulated plate response under these distributed loads, where the specific impulse distributions were applied as equivalent initial nodal velocities. Note that uniform and energy equivalent uniform loads were not modelled in these examples. For each example, spherical charge models were also run with the equivalence factor set to $\pm 10\%$ the values determined from Figure 10 in order to assess the sensitivity of the method to small changes in equivalence factor. Converged mesh sizes from the parametric study (1 mm square axi-symmetric MMALE elements, 2 mm square Lagrangian shell elements for the two analysis parts respectively), were retained for the verification examples without modification since $W_C = 0.512$ kg, hence $SOD = 0.22 \times 0.512^{1/3} = 0.176$ m and actual target span is $0.50 \times 0.512^{1/3} = 0.40$ m).

The input parameters used in the verification study are summarised in Table 6. All span:thickness ratios (50, 40, and 32 respectively) satisfy the condition for thin plates (span:thickness > 20 [48]) and therefore it can be assumed that the plates deformed predominantly due to membrane action with minimal contribution from bending. The equivalence factors derived herein are invariant of plate thickness, provided this assumption is adhered to.

Table 6: Input parameters for verification examples

Ex.	Shape	L/D (-)	EF	W (kg)	L (mm)	D (mm)	SOD (m)	Z (m/kg ^{1/3})	t (mm)	Span (mm)
(i)	Cyl.	1.30	–	0.512	88.3	67.9	0.176	0.220	8.00	400
	Sph.	–	1.00	0.512	–	84.8	0.176	0.220	8.00	400
	Sph.	–	1.10 (+10%)	0.563	–	87.6	0.176	0.213	8.00	400
	Sph.	–	0.90 (–10%)	0.461	–	81.9	0.176	0.228	8.00	400
(ii)	Cyl.	0.80	–	0.512	63.9	79.8	0.176	0.220	10.0	400
	Sph.	–	1.60	0.819	–	99.2	0.176	0.188	10.0	400
	Sph.	–	1.76 (+10%)	0.901	–	102.4	0.176	0.182	10.0	400
	Sph.	–	1.44 (–10%)	0.737	–	95.8	0.176	0.195	10.0	400
(iii)	Cyl.	0.60	–	0.512	52.7	87.9	0.176	0.220	12.5	400
	Sph.	–	2.0	1.024	–	106.9	0.176	0.175	12.5	400
	Sph.	–	2.2 (+10%)	1.126	–	110.3	0.176	0.169	12.5	400
	Sph.	–	1.8 (–10%)	0.922	–	103.2	0.176	0.181	12.5	400

Figure 11 shows MMALE specific impulse distributions (a) and deflection-time histories at the centre of the plates (b) for all three verification examples (i–iii). It can be seen that whilst the loading distributions differ significantly, with the epicentral specific impulse from the cylindrical charges at least a factor of two greater than the epicentral specific impulse from the spherical charges in all examples, the resulting plate deflection histories are remarkably similar. Again, the plates under the cylindrical charge loading exhibit a more rapid rise to peak

deflection in each case relative to the spherical loading models, with a slightly lengthened post-peak oscillation period owing to small differences in the final deformed profiles of the plates.

Peak deflections from the verification exercises are shown in Table 7. The equivalent spherical displacements (with 1.0EF) differ from the cylindrical displacements by between 1–4% for all cases. Applying $\pm 10\%$ factors to the equivalence is shown here to provide an adequate margin of error, particularly when considering that practical examples may not align exactly with contour levels in Figure 10 and some interpolation/user-interpretation may be required. These verification exercises have offered an effective demonstration of the accuracy of the method derived in this article for determining spherical equivalence factors, even for combinations of Z and L/D which were not part of the original parameter study.

Table 7: Peak deflections from verification exercises

Ex.	Peak deflection (mm)			
	Cyl.	Sph.		
		1.0EF	1.1EF	0.9EF
(i)	41.82	39.97	46.52	34.29
(ii)	49.19	47.97	53.14	41.72
(iii)	54.76	54.35	61.56	46.23

6. Summary and conclusions

Quantification of the magnitude and distribution of the blast load acting on structural elements located close to an explosive charge is an essential first step in providing engineered protective systems. Here, the shape of the charge is known to significantly alter the imparted load, and simplified predictive methods which do not account for charge shape are unsuitable. There is a need to augment such simplified tools with physically valid adjustments to model the effects of charge shape.

This article aimed at developing a series of simple equivalence factors, defined as $EF = W_S/W_C$, where W_S and W_C are the mass of the spherical and cylindrical charges respectively. The equivalence factors were derived by equating the kinetic energy uptake [43]) from a cylindrical and equivalent spherical explosive located at the same stand off distance. Experimental data published in Ref. [32] was used to validate a two-part numerical modelling approach. Firstly, multi-material Arbitrary Lagrangian Eulerian analyses were performed to generate distributions

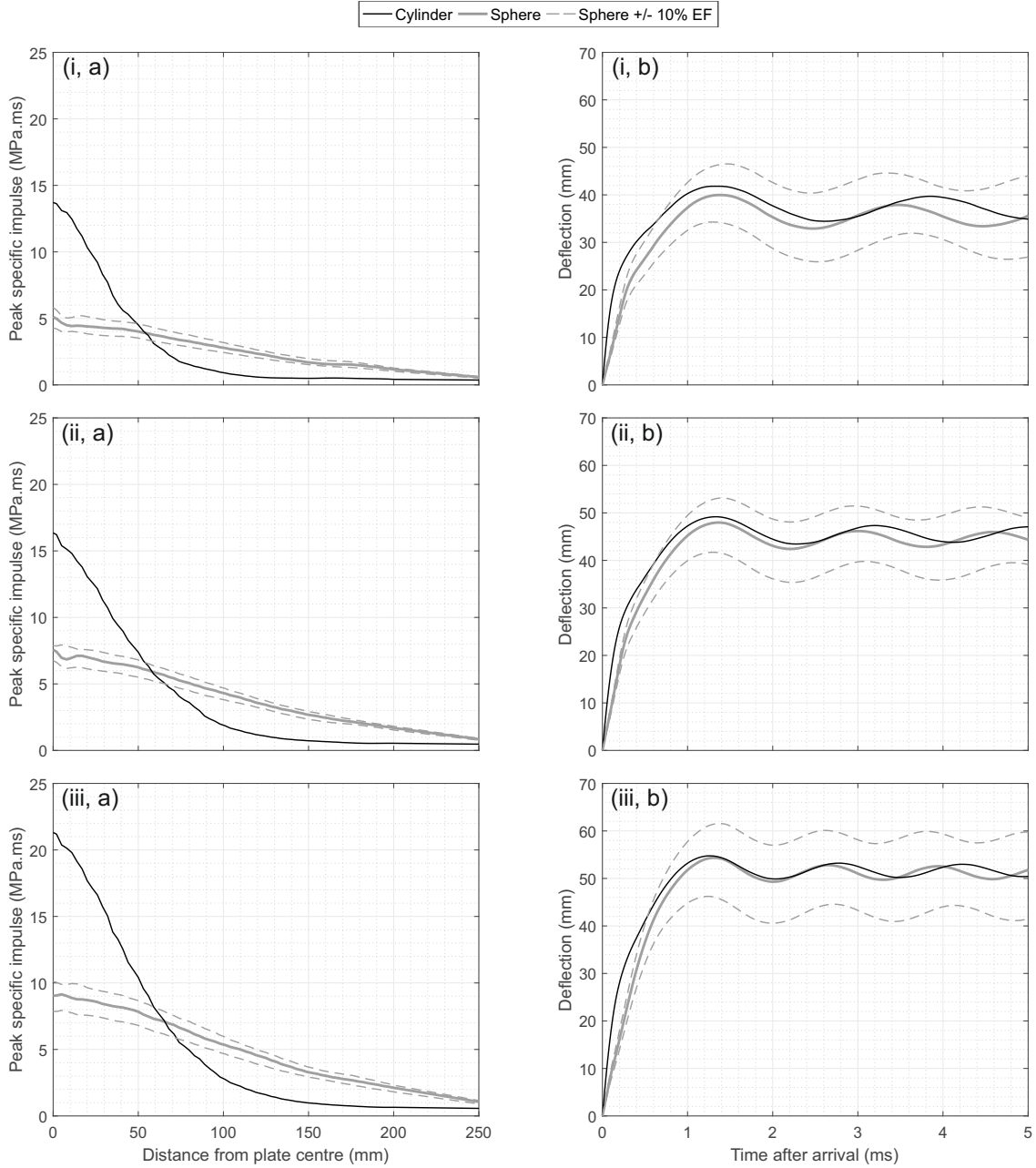


Figure 11: Results from verification examples: (a) MMALE model peak specific impulse, (b) Lagrangian model deflection. $W_C = 0.512$ kg, $Z = 0.220$ m/kg^{1/3}, and plate dimensions 400×400 mm throughout. (i) $L/D = 1.30$, $EF = 1.00$, $W_S = 0.512$ kg, $t = 8.00$ mm. (ii) $L/D = 0.80$, $EF = 1.60$, $W_S = 0.819$ kg, $t = 10.0$ mm. (iii) $L/D = 0.60$, $EF = 2.00$, $W_S = 1.024$ kg, $t = 12.5$ mm. See Table 6 for all input parameters in the verification examples

of specific impulse, which were then mapped on to Lagrangian plate models as initial velocity distributions in order to quantify plate deformation in the second stage of the analysis.

The validated modelling approach was used to perform a detailed parametric study, comprising 184 simulations in total, for $0.20 \leq L/D \leq 5$ and $0.108 \leq Z \leq 0.485 \text{ m/kg}^{1/3}$. For each charge configuration, plates were analysed under the distributed load (determined from part one of the analysis), as well as a uniform load (momentum-conserved, I) and an equivalent uniform load (energy-conserved, $I_{E,k}$). A high level of agreement was attained between the plates under the distributed and energy equivalent load, suggesting that transforming a distributed load into an energy equivalent uniform impulse (Equation 3) is a physically valid method for expressing a spatially varying load as a single-number equivalent. Furthermore, a strong linearity was shown to exist between initial kinetic energy and peak plate deflection.

Finally, kinetic energy uptake was evaluated for a large range of charge shapes (spherical and cylindrical: $0.2 \leq L/D \leq 5$), charge masses (unit for cylinders, $0.4 \leq W \leq 10 \text{ kg}$ for spheres using Hopkinson-Cranz scaling [64, 65]), scaled distances ($0.108 \leq Z \leq 0.485 \text{ m/kg}^{1/3}$ when scaled off the cylindrical charge mass), and scaled target sizes (0.25, 0.50 and $1.00 \text{ m/kg}^{1/3}$ when scaled off the cylindrical charge mass). In total, kinetic energy uptake was calculated for 168 cylindrical charge configurations and 2,592 spherical charge configurations ($9 \times \text{SODs}$, $96 \times \text{Ws}$, and 3 target sizes). For each cylindrical charge, logarithmic interpolation was used to determine the spherical mass required to impart the same kinetic energy at the same SOD for the same target size. The results were presented as contours of equivalence factor, plotted against scaled distance and aspect ratio, for the three target sizes considered. This method allows the engineer to use well established predictive tools, e.g. ConWep [7], with a relatively simple adjustment to model the effects of a non-spherical charge.

A series of verification examples were devised, which showed that modelling a cylindrical charge as an equivalent spherical charge resulted in a deflection that matched the cylindrical model to within $\sim 4\%$, and it is suggested that $\pm 10\%$ on the factors determined from Figure 10 should adequately account for inaccuracies in determining spherical equivalence from the charts.

The method developed herein is based on sound physical principles which incorporate the effects of loading distribution across the entire reflecting surface (as opposed to a single point), and is informed by detailed and rigorous numerical modelling with clearly demonstrated accuracy and validity. The proposed method is applicable for situations where central deflections are several times greater than plate thickness, membrane strains that arise

from out of plane displacements are assumed to dominate, and failure does not occur ($\phi < 28$). Such an approach is suitable for use beyond the spherical/cylindrical equivalence derived in this manuscript, and can conceivably be used to develop equivalence between any two systems which each possess a complex distributed loading function.

References

- [1] I.D. Elgy, S.D. Clarke, B.J. Fuller, A.D. Barr, D.W. Armstrong, M.T.A. Gant, J.J. Keirl, G.C.E. Porter, I.D. Softly, and A. Tyas. Deformation of ArmoX 440T plates subject to buried explosive charge detonations: A benchmark for appliqué systems. *International Journal of Impact Engineering*, 150:103819, 2021.
- [2] H. Dirlwanger, D. Pope, D. Russell, F. Landmann, C. Haberacker, A.D. Barr, A. Tyas, and A. Stoltz. Enhancement of Hesco Bastion wall models to better predict magnitudes of response under far field loading conditions. In *Proceedings of The 17th International Symposium for the Interaction of Munitions with Structures (ISIEMS17)*, Bad Neuenahr, Germany, 2017.
- [3] D. Cormie, G. Mays, and P. Smith. *Blast effects on buildings, 2nd ed.* Thomas Telford, London, UK, 2009.
- [4] H. L. Brode. Numerical solutions of spherical blast waves. *Journal of Applied Physics*, 26(6):766–775, 1955.
- [5] C. N. Kingery. *Airblast parameters versus distance for hemispherical TNT surface bursts*. ARBRL-TR-1344, US Army Ballistic Research Laboratory, Aberdeen Proving Ground, MD, USA, 1966.
- [6] C. N. Kingery and G. Bulmash. *Airblast parameters from TNT spherical air burst and hemispherical surface burst*. ARBRL-TR-02555, US Army Ballistic Research Laboratory, Aberdeen Proving Ground, MD, USA, 1984.
- [7] D W. Hyde. *Conventional Weapons Effect Program (ConWep)*. U.S Army Waterways Experimental Station, Vicksburg, MS, USA, 1991.
- [8] S.E. Rigby, A. Tyas, S. D. Fay, S. D. Clarke, and J. A. Warren. Validation of semi-empirical blast pressure predictions for far field explosions – is there inherent variability in blast wave parameters? In *6th International Conference on Protection of Structures Against Hazards (PSH14)*, Tianjin, China, 2014.
- [9] J. J. Pannell, G. Panoutsos, S. B. Cooke, D. J. Pope, and S. E. Rigby. Predicting specific impulse distributions for spherical explosives in the extreme near-field using a Gaussian function. *International Journal of Protective Structures*, 2021.
- [10] C. Knock and N. Davies. Blast waves from cylindrical charges. *Shock Waves*, 23:337–343, 2013.
- [11] J. K. Clutter and M. W. Stahl. Effect of charge shape on damage from potential explosive attacks. In *6th International Conference on Protection of Structures Against Hazards (PSH14)*, Tianjin, China, 2014.
- [12] E. D. Esparza. Spherical equivalency of cylindrical charges in free-air. In *25th Department of Defense Explosives Safety Seminar*, Anaheim, CA, USA, 1992.

- [13] M. N. Plooster. *Blast front pressure from cylindrical charges of high explosives*. TM 3631, Naval Weapons Center, Denver Research Institute, China Lake, CA, USA, 1978.
- [14] D. K. Parks and G. S. Weeding. *Investigations of air blast parameters around cylindrical charges*. University of Denver, Denver Research Institute, CO, USA, 1959.
- [15] J. Wisotski and W. H. Snyder. *Characteristics of blast waves obtained from cylindrical high explosive charges*. University of Denver, Denver Research Institute, CO, USA, 1965.
- [16] M. N. Plooster. *Blast effects from cylindrical explosive charges: experimental measurements*. NWC TP 6382, Naval Weapons Center, Denver Research Institute, China Lake, CA, USA, 1982.
- [17] B. Simoens and M. Lefebvre. Influence of the shape of an explosive charge: quantification of the modification of the pressure field. *Central European Journal of Energetic Materials*, 12:195–213, 2015.
- [18] C. Wu, G. Fattori, A. Whittaker, and D. J. Oehlers. Investigation of air-blast effects from spherical-and cylindrical-shaped charges. *International Journal of Protective Structures*, 1(3):345–362, 2010.
- [19] P. Sherkar, J. Shin, A. Whittaker, and Aref A. Influence of charge shape and point of detonation on blast-resistant design. *Journal of Structural Engineering*, 142(2):04015109, 2016.
- [20] J. Artero-Guerrero, J. Pernas-Sánchez, and F. Teixeira-Dias. Blast wave dynamics: The influence of the shape of the explosive. *Journal of Hazardous Materials*, 331:189–199, 2017.
- [21] C. Langran-Wheeler, A. Tyas, S. E. Rigby, C. S. Stephens, S. Clarke, and J. Warren. Characterisation of reflected blast loads in the very-near field from non-spherical explosive charges. In *Proceedings of The 17th International Symposium for the Interaction of Munitions with Structures (ISIEMS17)*, Bad Neuenahr, Germany, 2017.
- [22] C. Langran-Wheeler, A. Tyas, S. Rigby, C. S. Stephens, S. Clarke, and R. E. Walker. Reflected blast loads from long cylinders in the near-field. In *Proceedings of The 18th International Symposium for the Interaction of Munitions with Structures (ISIEMS18)*, Panama City, FL, USA, 2019.
- [23] W. Xiao, M. Andrae, and N. Gebbeken. Effect of charge shape and initiation configuration of explosive cylinders detonating in free air on blast-resistant design. *Journal of Structural Engineering*, 146(8):04020146, 2020.
- [24] W. Xiao, M. Andrae, and N. Gebbeken. Influence of charge shape and point of detonation of high explosive cylinders detonated on ground surface on blast-resistant design. *International Journal of Mechanical Sciences*, 181:105697, 2020.
- [25] Y. Hu, L. Chen, Q. Fang, and H. Xiang. Blast loading model of the rc column under close-in explosion induced by the double-end-initiation explosive cylinder. *Engineering Structures*, 175:304–321, 2018.
- [26] C. Knock and N. Davies. Predicting the impulse from the curved surface of detonating cylindrical charges. *Propellants, Explosives, Pyrotechnics*, 36(2):105–109, 2011.

- [27] C. Knock and N. Davies. Predicting the peak pressure from the curved surface of detonating cylindrical charges. *Propellants, Explosives, Pyrotechnics*, 36(3):203–209, 2011.
- [28] C. Knock, N. Davies, and T. Reeves. Predicting blast waves from the axial direction of a cylindrical charge. *Propellants, Explosives, Pyrotechnics*, 40(2):169–179, 2015.
- [29] J. K. Clutter and K. W. King. Effect of charge shape on blast containment chamber survivability. *International Journal of Protective Structures*, 7(3):389–408, 2016.
- [30] A. Christian, L. R. Chandra, S. D. Adhikary, and K. C. G. Ong. Influence of charge shape and orientation on the response of steel-concrete composite panels. *International Journal of Engineering Technology and Innovation*, 6(4):284–293, 2016.
- [31] S. Chung Kim Yuen, A. Butler, H. Bornstein, and A. Cholet. The influence of orientation of blast loading on quadrangular plates. *Thin-Walled Structures*, 131:827–837, 2018.
- [32] S. E. Rigby, A. Tyas, R. J. Curry, and G. S. Langdon. Experimental measurement of specific impulse distribution and transient deformation of plates subjected to near-field explosive blasts. *Experimental Mechanics*, 59(2):163–178, 2019.
- [33] Y. Shi and . G. Stewart. Damage and risk assessment for reinforced concrete wall panels subjected to explosive blast loading. *International Journal of Impact Engineering*, 85:5–19, 2015.
- [34] G. N. Nurick, S. Mahoi, and G. S. Langdon. The response of plates subjected to loading arising from the detonation of different shapes of plastic explosive. *International Journal of Impact Engineering*, 89:102–113, 2016.
- [35] SA Davids, GS Langdon, and G.N. Nurick. The influence of charge geometry on the response of partially confined right circular stainless steel cylinders subjected to blast loading. *International Journal of Impact Engineering*, 108:252–262, 2017.
- [36] L. Bortolan Neto, M. Saleh, V. Pickerd, G. Yiannakopoulos, Z. Mathys, and W. Reid. Rapid mechanical evaluation of quadrangular steel plates subjected to localised blast loadings. *International Journal of Impact Engineering*, 137:103461, 2020.
- [37] N. Jacob, S. Chung Kim Yuen, G.N. Nurick, D. Bonorchis, S.A. Desai, and D. Tait. Scaling aspects of quadrangular plates subjected to localised blast loadsexperiments and predictions. *International Journal of Impact Engineering*, 30(8):1179–1208, 2004.
- [38] S. K. Nayak, A. K. Singh, A. D. Belegundu, and C. F. Yen. Process for design optimization of honeycomb core sandwich panels for blast load mitigation. *Structural and Multidisciplinary Optimization*, 47(5):749–763, 2013.
- [39] Y. Wang, W. Zhao, G. Zhou, and C. Wang. Analysis and parametric optimization of a novel sandwich panel with double-v auxetic structure core under air blast loading. *International Journal of Mechanical Sciences*, 142–143:245–254, 2018.
- [40] T. Liu, G. Sun, J. Fang, J. Zhang, and Q. Li. Topographical design of stiffener layout for plates against blast loading using a modified ant colony optimization algorithm. *Structural and Multidisciplinary Optimization*, 59(2):335–350, 2019.
- [41] E. Wang, Q. Li, and G. Sun. Computational analysis and optimization of sandwich panels with homogeneous and graded foam cores for blast resistance. *Thin-Walled Structures*, 147:106494, 2020.

- [42] J. O. Hallquist. *LS-DYNA Theory Manual*. Livermore Software Technology Corporation, CA, USA, 2006.
- [43] S. E. Rigby, O. I. Akintaro, B. J. Fuller, A. Tyas, R. J. Curry, G. S. Langdon, and D. J. Pope. Predicting the response of plates subjected to near-field explosions using an energy equivalent impulse. *International Journal of Impact Engineering*, 128:24–36, 2019.
- [44] S. E. Rigby, R. J. Curry, G.S. Langdon, and A. Tyas. Initial velocity and impulse distribution of blast loaded plates. In *Proceedings of the 17th International Symposium on Interaction of the Effects of Munitions with Structures (ISIEMS17)*, Bad Neuenahr, Germany, 2017.
- [45] C. K. Youngdahl. Correlation parameters for eliminating the effect of pulse shape on dynamic plastic deformation. *Journal of Applied Mechanics*, 37:744–752, 1970.
- [46] N. Jones. *Structural Impact*. Cambridge University Press, UK, 1990.
- [47] N. Jones. Impulsive loading of a simply supported circular rigid plastic plate. *Journal of Applied Mechanics*, 35(1):59–65, 1968.
- [48] C.R. Steele and C.D. Balch. *Introduction to the theory of plates*. Department of Mechanical Engineering, Stanford University, CA, USA, 2009.
- [49] S. E. Rigby, B. J. Fuller, and A. Tyas. Validation of near-field blast loading in LS-DYNA. In *Proceedings of the 5th International Conference on Protective Structures (ICPS5)*, Poznan, Poland, 2018.
- [50] B. Fuller, S. E. Rigby, A. Tyas, S. D. Clarke, S. D. Fay, J. J. Reay, J. A. Warren, and I. Elgy. Effect of spatial variation of blast loading on response of plates. In *Proceedings of the First International Conference on Structural Safety Under Fire & Blast (CONFAB)*, Glasgow, Scotland, 2015.
- [51] A. Remennikov, T. Ngo, D. Mohotti, B. Uy, and M. Netherton. Experimental investigation and simplified modeling of response of steel plates subjected to close-in blast loading from spherical liquid explosive charges. *International Journal of Impact Engineering*, 101:78–89, 2017.
- [52] R. J. Curry and G. S. Langdon. Transient response of steel plates subjected to close proximity explosive detonations in air. *International Journal of Impact Engineering*, 102:102–116, 2017.
- [53] E. L. Lee, H. C. Hornig, and J. W. Kury. *Adiabatic expansion of high explosive detonation products*. TID 4500-UCRL 50422, Lawrence Radiation Laboratory, University of California, CA, USA, 1968.
- [54] D. Bogosian, M. Yokota, and S. Rigby. TNT equivalence of C-4 and PE4: A review of traditional sources and recent data. In *24th International Symposium on Military Aspects of Blast and Shock (MABS24)*, Halifax, Nova Scotia, Canada, 2016.
- [55] B. M. Dobratz and P. C. Crawford. *LLNL explosives handbook - properties of chemical explosives and explosive simulants*. UCRL 52997, Lawrence Livermore National Laboratory, University of California, CA, USA, 1985.
- [56] C. Osborne. *Spherical equivalency of cylindrical charges derived from plate deformation*. MEng Dissertation, Department of Civil and Structural Engineering, University of Sheffield, United Kingdom, 2020.

- [57] C. Geretto. *The Effects of Different Degrees of Confinement on the Deformation of Square Plates Subjected to Blast Loading*. PhD thesis, Department of Mechanical Engineering, University of Cape Town, South Africa, 2012.
- [58] G. R. Johnson and W. H. Cook. Constitutive model and data for metals subjected to large strains, high strain rates and high temperatures. In *Proceedings of the 7th International Symposium on Ballistics, The Hague, The Netherlands*, 1983.
- [59] R. Curry. *Response of plates subjected to air-blast and buried explosions*. PhD thesis, Department of Mechanical Engineering, University of Cape Town, South Africa, 2017.
- [60] H. Y. Grisaro, I. E. Edri, and S. Rigby. TNT equivalency analysis of specific impulse distribution from close-in detonations. *International Journal of Protective Structures*, 2020.
- [61] G. Nurick and J. Martin. Deformation of thin plates subjected to impulsive loading – a review. Part 2: experimental studies. *International Journal of Impact Engineering*, 8:171–186, 1989.
- [62] J. M. Biggs. *Introduction to Structural Dynamics*. McGraw-Hill, New York, NY, USA, 1964.
- [63] T.J. Cloete and G.N. Nurick. On the influence of radial displacements and bending strains on the large deflections of impulsively loaded circular plates. *International Journal of Mechanical Sciences*, 82:140–148, 2014.
- [64] B. Hopkinson. *British Ordnance Board Minutes, 13565*. 1915.
- [65] C. Cranz. *Lehrbuch der Basllistik*. Springer, Berlin, Germany, 1926.